Supercurrent rectification and magnetochiral effects in symmetric Josephson junctions

Christian Baumgartner[1,8], Lorenz Fuchs[1,8], Andreas Costa [2], Simon Reinhardt [1], Sergei Gronin[3,4], Geoffrey C. Gardner [3,4], Tyler Lindemann[4,5], Michael J. Manfra [3,4,5,6,7], Paulo E. Faria Junior[2], Denis Kochan[2], Jaroslav Fabian [2], Nicola Paradiso [1✉] and Christoph Strunk [1]

Transport is non-reciprocal when not only the sign, but also the absolute value of the current depends on the polarity of the applied voltage. It requires simultaneously broken inversion and time-reversal symmetries, for example, by an interplay of spin–orbit coupling and magnetic field. Hitherto, observation of nonreciprocity was tied to resistivity, and dissipationless non-reciprocal circuit elements were elusive. Here we engineer fully superconducting non-reciprocal devices based on highly transparent Josephson junctions fabricated on InAs quantum wells. We demonstrate supercurrent rectification far below the transition temperature. By measuring Josephson inductance, we can link the non-reciprocal supercurrent to an asymmetry of the current–phase relation, and directly derive the supercurrent magnetochiral anisotropy coefficient. A semiquantitative model explains well the main features of our experimental data. Non-reciprocal Josephson junctions have the potential to become for superconducting circuits what pn junctions are for traditional electronics, enabling new non-dissipative circuit elements.

The pn junction[1,2] is a key component of modern electronics, being the fundamental building block of devices such as LEDs, current rectifiers, voltage-controlled oscillators, photosensors and solar cells. Its working principle is the rectification effect produced by the spatial asymmetry of the junction, that is, the non-equivalence of the p and n leads. In spatially symmetric devices, the resistance depends instead on the current direction only if both inversion and time-reversal symmetry are simultaneously broken. This can be obtained, for example, by applying an electric and a magnetic field perpendicular to each other. In the linear response regime, the absence of both parity and time-reversal symmetry produces, by the Onsager relations[3–6], longitudinal transport coefficients that depend on the polarity of the current. This result can be extended[7,8] to the nonlinear regime and to diffusive two-dimensional (2D) conductors. If the electric field $\mathbf{E} \parallel \hat{\mathbf{e}}_z$ is directed out-of-plane, whereas the magnetic field $\mathbf{B}$ and current $\mathbf{I}$ are directed in-plane, the resistance can be written as

$$R = R_0[1 + \gamma \hat{\mathbf{e}}_z(\mathbf{B} \times \mathbf{I})]. \qquad (1)$$

In normal conductors, the magnetochiral anisotropy coefficient $\gamma = \gamma_N$ is usually tiny because the spin–orbit interaction (SOI) is typically many orders of magnitude smaller than the Fermi energy. However, in recent years several experiments have demonstrated a robust non-reciprocal charge transport in the fluctuation regime of noncentrosymmetric superconductors[9,10]. Here the energy scale, to which the SOI has to be compared with, is not the Fermi energy, but the superconducting gap. As a result, the resistance shows a sizeable magnetochiral anisotropy coefficient γ_S (refs. [5,6,9]). The observation of non-reciprocal transport in superconductors was so far confined

to a narrow temperature window near T_c, as it relies on measuring d.c. resistance, which vanishes at low temperatures. On the other hand, at low temperatures the supercurrent response to an a.c. excitation is described by its superfluid stiffness, which can be detected via kinetic inductance measurements. But does a magnetochiral anisotropy also exist for the superfluid? If it does, we may expect that it would be described by the analogue of equation (1),

$$L = L_0[1 + \gamma_L \hat{\mathbf{e}}_z(\mathbf{B} \times \mathbf{I})], \qquad (2)$$

with the resistance substituted for the kinetic inductance L. The magnetochiral anisotropy coefficient γ_L would then constitute a new observable that characterizes non-reciprocal supercurrents.

Magnetochiral anisotropy is expected to produce an intrinsic supercurrent diode effect in devices with spatially homogeneous supercurrent density, as opposed to the rectification observed in asymmetric superconducting quantum interference devices (SQUIDs) due to self-field effects[11,12].

In this work, we have engineered non-reciprocal superflow in synthetic noncentrosymmetric superconductors, that is, arrays of highly transparent Josephson junctions based on an InAs 2D electron gas (2DEG) proximitized by epitaxial Al. Using a recently demonstrated resonator technique[13], we measure the kinetic (or Josephson) inductance and investigate the effects of simultaneous inversion and time-reversal symmetry breaking on the current–phase relation (CPR). If the in-plane magnetic field has a component perpendicular to the current direction, a pronounced asymmetry appears in the current dependence of the Josephson inductance $L(I)$ that signals the magnetochiral anisotropy of the supercurrent, defined in equation (2). The supercurrent is different

[1]Institut für Experimentelle und Angewandte Physik, University of Regensburg, Regensburg, Germany. [2]Institut für Theoretische Physik, University of Regensburg, Regensburg, Germany. [3]Microsoft Quantum Purdue, Purdue University, West Lafayette, IN, USA. [4]Birck Nanotechnology Center, Purdue University, West Lafayette, IN, USA. [5]Department of Physics and Astronomy, Purdue University, West Lafayette, IN, USA. [6]School of Materials Engineering, Purdue University, West Lafayette, IN, USA. [7]School of Electrical and Computer Engineering, Purdue University, West Lafayette, IN, USA. [8]These authors contributed equally: Christian Baumgartner, Lorenz Fuchs. ✉e-mail: nicola.paradiso@physik.uni-regensburg.de
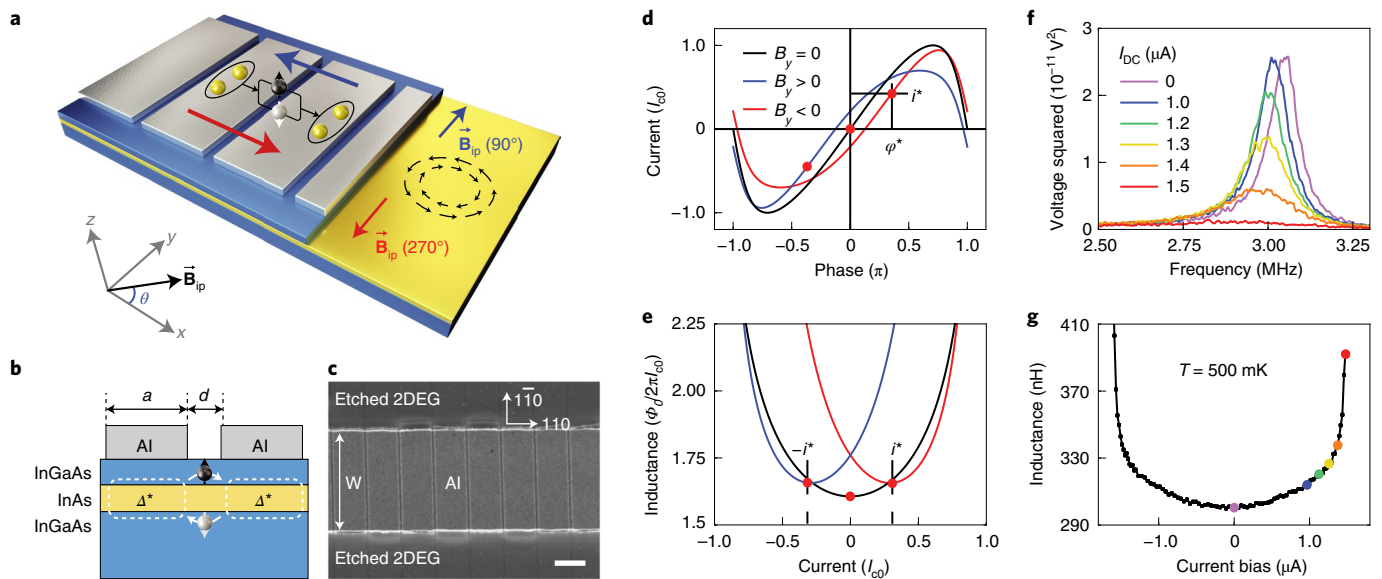
Fig. 1 | Josephson junction array and anomalous CPR. a, Sketch of Josephson junction array formed by a chain of Al islands (grey) on top of an InAs quantum well (yellow). Red and blue arrows denote the spontaneous supercurrents flowing at zero phase difference via spin-split pairs of ABS (black and white particle, representing electron and hole with opposite spin). Their strength and direction depend on that of a transverse magnetic field B_{ip}, which competes with the Rashba spin-texture (counterpropagating circles of black arrows) in the quantum well. The actual array is made of 2,250 islands of width $w = 3.15\,\mu m$ and length $a = 1.0\,\mu m$. The island separation is $d = 0.1\,\mu m$. **b**, Growth sequence for the heterostructure under study. The top Al layer induces an effective superconducting gap Δ^* in the InAs quantum well. **c**, Scanning electron micrograph of a part of the array, taken before the fabrication of a global top gate. Scale bar, 1 μm. **d**, Illustrative CPR for a short-ballistic Josephson junction with high transparency $\tau = 0.94$ and strong SOI in the absence (black) and presence of a transverse magnetic field $B_y \parallel \hat{y}$ (red, $B_y > 0$; blue, $B_y < 0$). In this example, the effect of finite $\pm B_y$ is to reduce by a factor 0.8 the critical current, $I_c = 0.8 I_{c0}$, and to add a cosinusoidal term $\pm 0.2 I_c \cos(\varphi)$ to the CPR's Fourier series. The red dots denote the inflection points (i^*, φ^*) of the CPR. **e**, Corresponding Josephson inductance as function of current. **f**, Resonance curves for the RLC circuit. The signal is the square of the voltage across the RLC tank[13], measured at 500 mK for different values of the current bias. **g**, Measured Josephson inductance $L(I)$ versus current at $B = 0$. Coloured symbols correspond to the spectra in **f**.

for opposite polarities of the phase difference, corresponding to a partial rectification of supercurrent.

Sample design

We fabricated devices, (Fig. 1a,b) starting from an InAs quantum well with a shallow 2DEG separated by a 10-nm-thick InGaAs barrier from a 7-nm-thick Al epitaxial film. The Al film induces in the 2DEG a superconducting gap Δ^* of about 130 μeV by proximity effect. We obtain superconductor–normal-superconductor Josephson junctions by patterning the Al film by electron-beam lithography and selective etching. The etching process leaves an array of N 3.15-μm-wide and 1.0-μm-long rectangular Al/2DEG islands separated by 3.15-μm-wide and 0.1-μm-long areas with the Al film stripped off, which serve as weak links. The scanning electron micrograph in Fig. 1c shows part of the array. The sample is embedded in a RLC circuit (a circuit containing a resistor, an inductor and a capacitor) that is integrated into the sample holder. The circuit allows us to measure both d.c. current–voltage (I–V) characteristics and sample inductance with a resolution of a fraction of nH. We deduce the inductance from the centre frequency shift of the RLC circuit resonance peak (Fig. 1f,g).

Skewed CPR and supercurrent diode effect

The 100-nm-long weak links in our samples are ballistic and close to the short-junction limit[13]. The supercurrent is therefore carried by one Kramers pair of Andreev bound states (ABS) per transverse mode. Their energy $\varepsilon_{ABS}(\varphi)$ depends on the phase difference φ between the superconducting leads. The phase derivative of the ABS spectrum eventually defines the CPR (black curve in Fig. 1d).

If either time-reversal symmetry (exchange of time direction) or parity symmetry (exchange of the leads) is preserved, then the ABS are symmetric, $\varepsilon_{ABS}(\varphi) = \varepsilon_{ABS}(-\varphi)$ and the CPR is antisymmetric, $I(\varphi) = -I(-\varphi)$, that is, its Fourier expansion contains only sinusoidal terms. The current is zero for zero phase difference, and vice versa. On the other hand, if both symmetries are broken, the Kramers degeneracy between the two spin components is also broken, as shown in Fig. 1d (red and blue curves). An anomalous CPR is thus observed[14–20], whose Fourier expansion contains also cosine terms. In experiments, this is typically revealed by measuring the anomalous phase shift φ_0 of the CPR in phase-biased junctions[21–24].

If, however, the junction transparency is high[13,23], higher harmonic sine terms appear in the CPR and the cosine terms introduced by the in-plane magnetic field cannot be absorbed in a mere phase shift. In this case, the positive and negative current branches in the CPR can be markedly different, as illustrated in Fig. 1d. This leads to two magnetoelectric effects, both demonstrated in the following sections: (1) the inflection point in the CPR occurs at a finite current i^* that changes sign when reversing the in-plane magnetic-field direction; and (2) the extremal values (that is, the critical currents I_c^- and I_c^+) for positive and negative phase difference differ, leading to a certain bias-current range in which a supercurrent diode effect can be measured: for one current direction, superflow is observed $(I < I_c^+)$, while for the other $(|I| > |I_c^-|)$ the junctions are in their resistive state. A 2DEG with Rashba SOI and in-plane field perpendicular to the current was one of the configurations predicted in ref.[25] to show an anomalous supercurrent. From the experimental point of view, this effect constitutes the Josephson junction
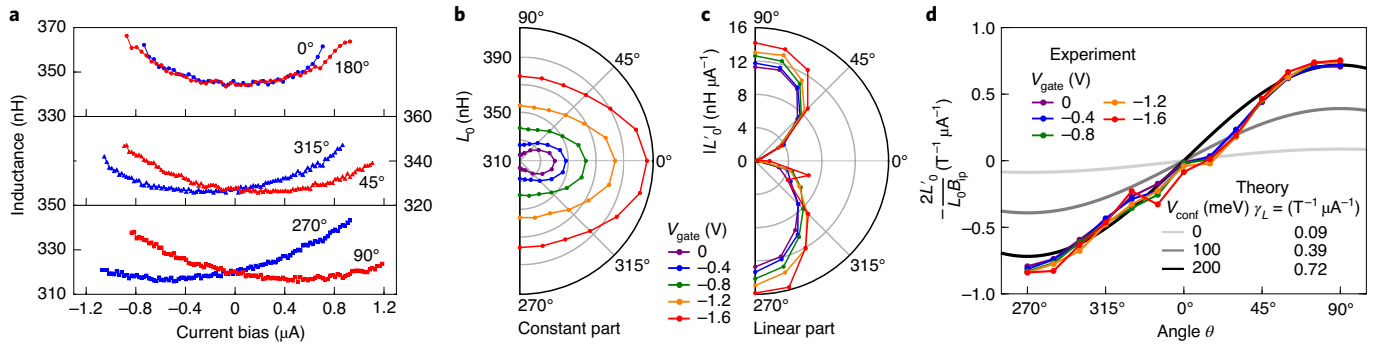
Fig. 2 | Supercurrent anisotropy and rectification. a, Current dependence of the kinetic inductance of the array for an applied in-plane magnetic field of 100 mT. The top graphs refer to an in-plane field directed parallel to the current direction $\hat{x}$. The middle graph refers to an in-plane magnetic field forming an angle of 45° with the current direction, while in the bottom graph the in-plane field is perpendicular to the current. Small vertical shifts have been applied to the curves to account for the residual field of the superconducting coil, as discussed in the Supplementary Information. **b,c**, Constant (**b**) and linear coefficients (**c**) of the polynomial expansion of $L(I)$ as a function of the angle θ between $\mathbf{B}_{ip}$ and the supercurrent density oriented along $\hat{x}$. **d**, Coloured lines and symbols show the measured supercurrent magnetochiral anisotropy $-2L_0'/(L_0 B_{ip})$ versus magnetic-field angle θ. A coefficient $\gamma_L = 0.77 \times 10^6\,\mathrm{T^{-1}\,A^{-1}}$ is extracted from a sine fit of the data. Grey scale lines are fitted magnetochiral anisotropy computed within our model for different values of the confinement potential V_{conf}. The corresponding values of the maximum magnetochiral anisotropy γ_L are reported. The three curves are perfect sine functions. All measurements have been performed at $T = 100\,\mathrm{mK}$.

analogue of the supercurrent rectification recently reported in ref. [26] for 2D metallic superlattices.

Magnetochiral anisotropy for supercurrents

A convenient probe of the CPR symmetry is the Josephson inductance, which can be derived by combining the CPR $I = I_{c0}f(\varphi)$ and the second Josephson equation $\dot{\varphi} = 2eV/\hbar$ to

$$ L = \frac{V}{\mathrm{d}I/\mathrm{d}t} = \frac{\hbar}{2eI_{c0}\frac{\mathrm{d}f(\varphi)}{\mathrm{d}\varphi}} = \frac{\hbar}{2e}\frac{\mathrm{d}\varphi(I)}{\mathrm{d}I}. \qquad (3) $$

The Josephson inductance is proportional to the derivative of the inverse CPR. Therefore, the minimum of $L(I)$ occurs at the inflection-point current i^* in the CPR (red dot on blue curve in Fig. 1e). As shown in the corresponding reference measurement in Fig. 1g, $L(I)$ is symmetric around zero current, where the minimum inductance occurs in the absence of magnetic fields. The situation can change when an in-plane field is added, as shown in Fig. 2a. If the in-plane field $\mathbf{B}_{ip} = B_x\hat{x} + B_y\hat{y}$ is parallel to the current ($B_y = 0$), no asymmetry is observed (top panel in Fig. 2a). The overall inductance increases, reflecting the gap (and thus the critical current) reduction, but no magnetochiral effect is observed, as the vector product $\mathbf{B} \times \mathbf{I}$ is still zero. On the contrary, when the in-plane field has a component B_y perpendicular to the current, a clear asymmetry is observed: the minimum of $L(I)$ (corresponding to the inflection point in the CPR) occurs now at a finite current i^*. The value of i^* increases with increasing B_y and its sign switches together with the sign of B_y.

To quantify the effect, we take the leading terms in the polynomial expansion of $L(I) \approx L_0 + L'I + L''I^2/2$ around zero current, with $L' \equiv \partial_I L|_{I=0}$ and $L'' \equiv \partial_I^2 L|_{I=0}$. In Fig. 2b,c, we plot the constant term L_0 and the linear term L' as functions of the angle between the applied in-plane field $\mathbf{B}_{ip}$ and the current direction $\hat{x}$. The constant term increases in magnitude when decreasing gate voltage towards more negative values and shows relatively small anisotropy. The increase of L_0 reflects the decrease of I_{c0} with decreasing number of channels. The slight anisotropy of L_0 probably reflects a warping of the Fermi surface in the parallel field that affects the Fermi velocities of the two spin components. In contrast, the linear term is strongly anisotropic, as it vanishes for magnetic fields parallel to the current direction and reaches its maximum for transverse field

($B_x = 0$). Very similar results have been found for a second sample with current flow in the [1$\bar{1}$0] direction. Figure 2d shows that the ratio L_0'/L_0 is nearly independent of the gate voltage and varies in good approximation proportionally to $(\mathbf{B} \times \mathbf{I}) \cdot \hat{z} = BI\sin\theta$, where θ is the angle between $\mathbf{B}_{ip}$ and $\mathbf{I}$. From the amplitude of the sine, we extract the magnetochiral anisotropy coefficient for the inductance, $\gamma_L = 0.77 \times 10^6\,\mathrm{T^{-1}\,A^{-1}}$. This is a new observable that refers directly to the superfluid and cannot be detected by resistance measurements. It is of the same order of the corresponding coefficient γ_S for the resistance discussed below, namely, in the range of $10^6\,\mathrm{T^{-1}\,A^{-1}}$.

To numerically simulate the $L(I)$ characteristics of the Josephson junction array and to extract the supercurrent magnetochiral anisotropy coefficient, we developed a realistic theoretical model (see Supplementary Information for further details) whose KWANT[27] implementation provides a semiquantitative description of our experimental data. The fundamental parameters in our model are the Bychkov–Rashba spin–orbit coupling strength $\alpha = 15\,\mathrm{meV\,nm}$ (see Supplementary Information for further details)[28], the in-plane g-factor $g^* \cong -10$ of the InAs quantum well[28], the effective mass of electrons $m^* \cong 0.02m_0$ (m_0 is the free-electron mass)[29,30], as well as the Fermi energy that we estimated as $\mu \cong 239\,\mathrm{meV}$. We approximate the effects of charge transfer and band alignment within the InAs layer by a parabolic potential well of depth V_{conf}. This parameter controls the magnitude of the anisotropy with respect to the orientation of the in-plane magnetic field. The ratio of the Zeeman shift of the two spin subbands to the Fermi energy μ controls the orbital phase shift between the subbands forming the ABS[16–18]. Hence, the Zeeman shifts become more important at low μ (and thus high V_{conf}). The lower the Fermi level, the lower the $\hat{x}$-component of the Fermi velocity, and thus the higher the CPR asymmetry[15]. As discussed in the Supplementary Information, the effect is amplified in the presence of many transverse channels in wide junctions: modes with large transverse wavevector $k_{F,y}$ must have a low longitudinal $k_{F,x}$. These modes contribute overproportionally to the anomalous CPR shift φ_0 (ref. [23]).

The results of our numerical simulations are also shown in Fig. 2d and fully support our qualitative reasoning. In particular, the sinusoidal dependence of $L_0'(\theta)$ on the in-plane angle θ is nicely reproduced. Assuming $V_{conf} = 0$, we obtain supercurrent magnetochiral anisotropy coefficients γ_L that are about one order of magnitude lower than the experimentally detected ones. Since the anisotropy increases linearly with the Rashba parameter (analogously to φ_0,
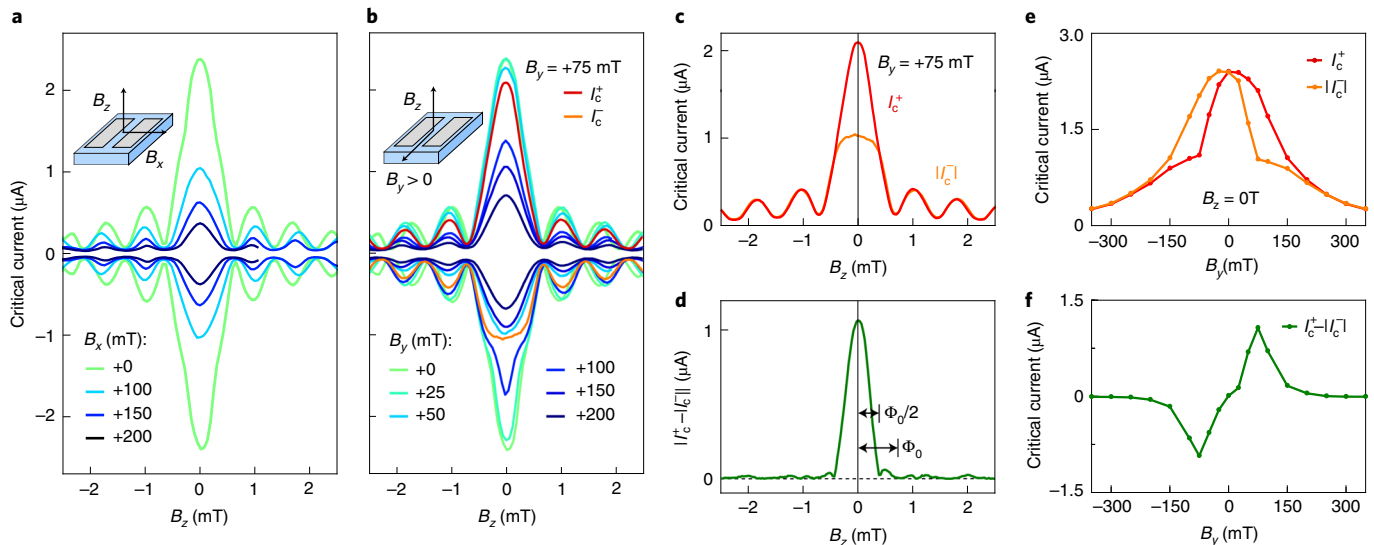
Fig. 3 | Supercurrent interference. a, Fraunhofer patterns of the Josephson junction array in combined out-of-plane B_z and in-plane magnetic field B_x parallel to the current flow, with $B_y = 0$. Each curve represents the critical current $I_c(B_z)$ at a given value of B_x. **b**, Modified Fraunhofer patterns for in-plane fields $B_y > 0$ transverse to the current flow, with $B_x = 0$. **c**, Direct comparison of I_c^+ and $|I_c^-|$ versus B_z for $B_y = 75$ mT, where the asymmetry is the largest. **d**, Measured $|\Delta I_c| \equiv |I_c^+ - |I_c^-||$. The diode effect is suppressed whenever the applied flux equals a multiple of $\Phi_0/2 \cong 0.37$ mT as discussed in the Supplementary Information. **e**, I_c^+ and $|I_c^-|$ as a function of B_y for $B_z = 0$. **f**, Difference between I_c^+ and $|I_c^-|$ for the latter case. All measurements have been performed at $T = 100$ mK.

ref. [15]) (see Supplementary Information for further details), reproducing the experimental values would require its enhancement by approximately one order of magnitude, which is unrealistic. Instead, we assume a finite confinement potential V_{conf}, which we estimate to be about 200 meV from the comparison with the measured data. This value is not far from the 150 meV value reported in an earlier work for the confinement in symmetric AlGa/GaAs/AlGa multilayers[31]. Our model reproduces within a factor of four the normal-state Sharvin resistance of the channel. This consistency indicates that the measured value of γ_L, the new quantity introduced in this work, can be justified at a microscopic level using reasonable material parameters.

The kinetic inductance reveals a magnetochiral anisotropy deep in the superconducting state, which is consistent with equation (2). The asymmetry with respect to the current is ultimately produced by the combination of orthogonal electric (leading to Rashba SOI) and magnetic fields that are both perpendicular to the current direction. Therefore, this is the superfluid analogue of the magnetochiral effect for the resistance observed in the fluctuation regime of noncentrosymmetric superconductors[9,10].

Josephson junction rectifiers

To check for the second magnetoelectric effect—the anomalous critical currents I_c^+ and I_c^-—we have measured supercurrent interference patterns by applying a small out-of-plane magnetic field $\mathbf{B}_z \parallel \hat{z}$ coexisting with the in-plane field $\mathbf{B}_{ip} = B_x\hat{x} + B_y\hat{y}$, whose magnitude and orientation with respect to the current direction can be controlled. The results are shown in Fig. 3a,b. The different curves show the positive I_c^+ and negative I_c^- critical currents displayed as a function of the out-of-plane magnetic field in the upper and lower half-planes, respectively. For both current orientations, the d.c. bias was swept from zero to finite (positive or negative) values. In this way, a heating-induced hysteresis of the switching current is excluded. The critical current was determined as the current bias producing a threshold voltage of roughly 1 µV per junction (2 mV in total).

In the absence of in-plane fields, the pattern is symmetric and Fraunhofer-like[23,32,33], as shown in Fig. 3a. In this case, as discussed

in ref. [13], the Fraunhofer pattern of the Josephson junction array behaves exactly as expected for a series of independent single junctions. The introduction of an in-plane field parallel to the current reduces the gap and thus the critical current, but does not introduce any asymmetry between the positive and negative current directions. Besides some variations of the apparent period of the patterns with B_{ip} (see Supplementary Information for further details), the lobe structure is close to the standard Fraunhofer shape.

On the other hand, in the presence of a transverse in-plane field component B_y (perpendicular to the current), a clear asymmetry between positive and negative current bias is observed, as shown in Fig. 3b. By inverting the sign of B_y a nearly identical graph is produced, but with the sign of the ordinates inverted (Extended Data Fig. 1). A striking consequence of such asymmetry is the superconducting diode effect, which manifests itself in the difference $\Delta I_c \equiv I_c^+ - |I_c^-|$ between the critical currents (I_c^+ and I_c^-) corresponding to the two current polarities. In the current range between $|I_c^-|$ and $|I_c^+|$, supercurrent can only flow in one direction, controllable through the in-plane magnetic field[26]. To highlight the diode effect, we select the diffraction patterns for $B_y = +75$ mT and both current polarities I_c^+ and $|I_c^-|$ from Fig. 3b (red and orange curves in Fig. 3c). The absolute value of ΔI_c is plotted in Fig. 3d. We notice here that the diode effect first vanishes at about half of the main lobe and it is modulated with a period corresponding to half flux quantum, that is to $\Phi_0/2 \cong 0.37$ mT. The reason for this phenomenology can be traced back to the main requirement for the observation of diode effect in Josephson junctions, namely, the presence of higher harmonics in the Fourier expansion of the CPR, which must then be non-sinusoidal already in absence of field. In the Supplementary Information and in the Extended Data Fig. 2 we show that for a typical rectangular, short-ballistic Josephson junction[34,35] the higher harmonics are periodically suppressed as function of B_z, with a period corresponding to Φ_0/n, with n being the order of the harmonic term. Since the most relevant higher order term is that for $n = 2$ (with Fourier coefficient b_2, see Supplementary Information for further details), we expect the diode effect to be suppressed with a period $\Phi_0/2$. More precisely, the modulation of $|\Delta I_c|$ follows the
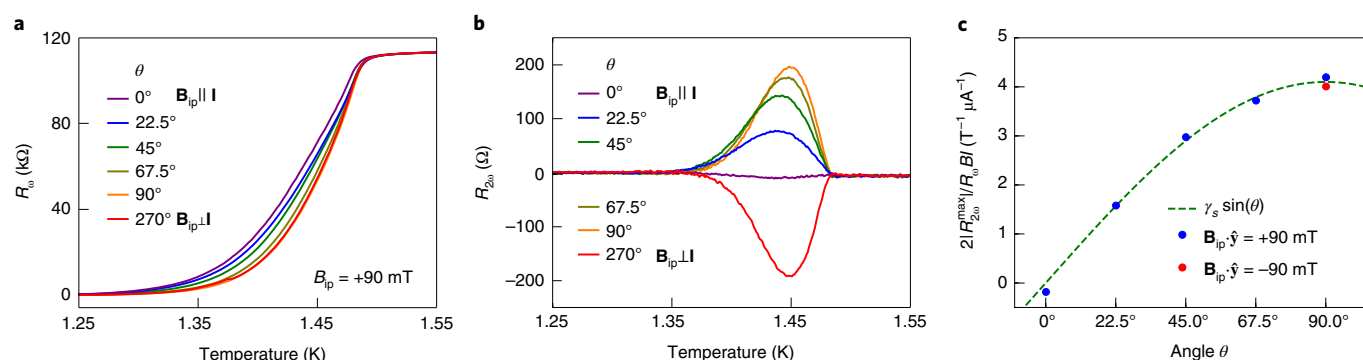
Fig. 4 | Magnetochiral anisotropy in the fluctuation regime. a, Resistive transition $R_\omega(T,\theta)$ for different angles θ of the in-plane magnetic field. This measurement has been performed on another array. **b**, Second harmonics $R_{2\omega}(T,\theta) = V_{2\omega}(T,\theta)/I_{ac}$ of the $V(I)$ characteristics. The a.c. current bias is $I_{ac} = 20$ nA. **c**, Fluctuation magnetochiral anisotropy $2R_{2\omega}^{max}/R_\omega$ versus in-plane angle θ. $R_{2\omega}^{max}$ are the maxima in **b** and R_ω the corresponding linear resistance. The data point in red is obtained by inverting the direction of $\mathbf{B}_{ip}$, which is equivalent to setting $\theta = 270°$. The experimental error is smaller or comparable to the symbol size. The coefficient $\gamma_S = 4.1 \times 10^6$ T^{-1} A^{-1} is extracted from a sine fit of the data.

product $I_c(B_z)|b_2(B_z)|$ very well (see Supplementary Information for further details).

Figure 3e shows the corresponding data versus transverse in-plane field B_y (red and orange curves) for $B_z = 0$. Again, to highlight the supercurrent diode effect, in Fig. 3f we plot the critical current difference ΔI_c. Up to a breakdown field of about 80 mT, the diode effect is linear in the transverse in-plane field B_y (equation (2)). The rapid quenching of the rectification is due to the suppression of the higher harmonics at higher temperature (see Supplementary Information for further details). We emphasize that the diode effect is, as expected, observed in the low temperature limit $k_B T \ll \Delta$.

Magnetochiral anisotropy of the resistance

It is interesting to check whether our Josephson junctions also display a magnetochiral anisotropy of the resistance in the regime of thermal phase fluctuations close to T_c. A convenient way to measure the effect[9,10,36,37] is by lock-in techniques. A linear variation of the differential resistance on the current (and thus a quadratic term in the voltage–current characteristic $V(I)$) can be detected measuring the 2ω voltage response to a sinusoidal current excitation at frequency ω. We expect the effect to be negligible both at temperatures well above T_c ($\gamma_N \ll \gamma_S$) and below T_c (no measurable resistance, $R_0 = 0$). Figure 4a,b show, respectively, the linear (R_ω) and the quadratic ($R_{2\omega}$) contribution to $V(I)$ as a function of temperature and for different in-plane fields. As expected, we observe a finite magnetochiral anisotropy coefficient $\gamma_S \simeq 4.1 \times 10^6$ T^{-1} A^{-1} near the transition temperature. The product between γ_S and sample width is about 12.9 T^{-1} A^{-1} m, similar (see Supplementary Information for further details) to that recently reported in the phase-fluctuation regime of 2D interfacial superconductors[10]. As shown in Fig. 4c, the nonlinear resistance is proportional to the field component perpendicular to the current direction. By rotating the sample with respect to the magnetic field, we clearly see a sinusoidal variation with the angle θ between current and field, as expected from equation (1).

Conclusions

In conclusion, we have demonstrated that Josephson junctions with Rashba SOI display a strong supercurrent magnetochiral anisotropy and a corresponding supercurrent diode effect. We have shown that higher harmonics in the CPR are crucial in breaking the symmetry between the positive and negative branches, leading to a supercurrent diode effect instead of a simple anomalous phase shift. Deep in the superconducting regime, we have characterized the magnetochiral anisotropy effect for the supercurrent via Josephson inductance

measurements as a function of the three components of the magnetic field. Experimental data compare well with the results of tight-binding simulations based on realistic material parameters for epitaxial Al/InAs 2DEGs. Our measurements show that both the inductance in the dissipationless regime and the resistance in the dissipative phase-fluctuation regime contain a correction term, which is bilinear in both field and current. The magnetochiral anisotropy coefficient for the supercurrent is a new observable introduced in this work. Instead, the corresponding coefficient for the resistance is a known quantity already measured in 2D superconductors in the phase-fluctuation regime. Despite the different physical playground, the value we measured for InAs quantum well is quantitatively similar to that reported for superconducting 2D materials. Our results extend the study of non-reciprocal transport to the realm of superfluids. Spatially symmetric Josephson junctions act as controllable supercurrent rectifiers, which may find applications in microwave quantum electronic circuits.

Online content

Any methods, additional references, Nature Research reporting summaries, source data, extended data, supplementary information, acknowledgements, peer review information; details of author contributions and competing interests; and statements of data and code availability are available at https://doi.org/10.1038/s41565-021-01009-9.

References

1. Scaff, J. H. & Ohl, R. S. Development of silicon crystal rectifiers for microwave radar receivers. *Bell Syst. Tech. J.* **26**, 1–30 (1947).
2. Shockley, W. The theory of p–n junctions in semiconductors and p–n junction transistors. *Bell Syst. Tech. J.* **28**, 435–489 (1949).
3. Onsager, L. Reciprocal relations in irreversible processes. I. *Phys. Rev.* **37**, 405–426 (1931).
4. Kubo, R. Statistical-mechanical theory of irreversible processes. I. General theory and simple applications to magnetic and conduction problems. *J. Phys. Soc. Jpn* **12**, 570–586 (1957).
5. Tokura, Y. & Nagaosa, N. Nonreciprocal responses from non-centrosymmetric quantum materials. *Nat. Commun.* **9**, 3740 (2018).
6. Hoshino, S., Wakatsuki, R., Hamamoto, K. & Nagaosa, N. Nonreciprocal charge transport in two-dimensional noncentrosymmetric superconductors. *Phys. Rev. B* **98**, 054510 (2018).
7. Rikken, G. L. J. A., Fölling, J. & Wyder, P. Electrical magnetochiral anisotropy. *Phys. Rev. Lett.* **87**, 236602 (2001).
8. Rikken, G. L. J. A. & Wyder, P. Magnetoelectric anisotropy in diffusive transport. *Phys. Rev. Lett.* **94**, 016601 (2005).

9. Wakatsuki, R. et al. Nonreciprocal charge transport in noncentrosymmetric superconductors. *Sci. Adv.* **3**, e1602390 (2017).

10. Itahashi, Y. M. et al. Nonreciprocal transport in gate-induced polar superconductor SrTiO₃. *Sci. Adv.* **6**, eaay9120 (2020).

11. Fulton, T. A., Dunkleberger, L. N. & Dynes, R. C. Quantum interference properties of double Josephson junctions. *Phys. Rev. B* **6**, 855–875 (1972).

12. Barone, A. & Paterno, G. *Physics and Applications of the Josephson Effect* 2nd edn (John Wiley and Sons, Inc., 1982).

13. Baumgartner, C. et al. Josephson inductance as a probe for highly ballistic semiconductor-superconductor weak links. *Phys. Rev. Lett.* **126**, 037001 (2021).

14. Bezuglyi, E. V., Rozhavsky, A. S., Vagner, I. D. & Wyder, P. Combined effect of Zeeman splitting and spin-orbit interaction on the Josephson current in a superconductor-two-dimensional electron gas-superconductor structure. *Phys. Rev. B* **66**, 052508 (2002).

15. Buzdin, A. Direct coupling between magnetism and superconducting current in the Josephson φ_0 junction. *Phys. Rev. Lett.* **101**, 107005 (2008).

16. Reynoso, A. A., Usaj, G., Balseiro, C. A., Feinberg, D. & Avignon, M. Anomalous Josephson current in junctions with spin polarizing quantum point contacts. *Phys. Rev. Lett.* **101**, 107001 (2008).

17. Reynoso, A. A., Usaj, G., Balseiro, C. A., Feinberg, D. & Avignon, M. Spin-orbit-induced chirality of Andreev states in Josephson junctions. *Phys. Rev. B* **86**, 214519 (2012).

18. Yokoyama, T., Eto, M. & Nazarov, Y. V. Anomalous Josephson effect induced by spin-orbit interaction and Zeeman effect in semiconductor nanowires. *Phys. Rev. B* **89**, 195407 (2014).

19. Shen, K., Vignale, G. & Raimondi, R. Microscopic theory of the inverse Edelstein effect. *Phys. Rev. Lett.* **112**, 096601 (2014).

20. Konschelle, F., Tokatly, I. V. & Bergeret, F. S. Theory of the spin-galvanic effect and the anomalous phase shift φ_0 in superconductors and Josephson junctions with intrinsic spin-orbit coupling. *Phys. Rev. B* **92**, 125443 (2015).

21. Szombati, D. B. et al. Josephson φ_0-junction in nanowire quantum dots. *Nat. Phys.* **12**, 568–572 (2016).

22. Assouline, A. et al. Spin-orbit induced phase-shift in Bi₂Se₃ Josephson junctions. *Nat. Commun.* **10**, 126 (2019).

23. Mayer, W. et al. Gate controlled anomalous phase shift in Al/InAs Josephson junctions. *Nat. Commun.* **11**, 212 (2020).

24. Strambini, E. et al. A Josephson phase battery. *Nat. Nanotechnol.* **15**, 656–660 (2020).

25. Rasmussen, A. et al. Effects of spin-orbit coupling and spatial symmetries on the Josephson current in SNS junctions. *Phys. Rev. B* **93**, 155406 (2016).

26. Ando, F. et al. Observation of superconducting diode effect. *Nature* **584**, 373–376 (2020).

27. Groth, C. W., Wimmer, M., Akhmerov, A. R. & Waintal, X. Kwant: a software package for quantum transport. *New J. Phys.* **16**, 063065 (2014).

28. Mayer, W. et al. Superconducting proximity effect in InAsSb surface quantum wells with in situ Al contacts. *ACS Appl. Electron. Mater.* **2**, 2351–2356 (2020).

29. Vurgaftman, I., Meyer, J. R. & Ram-Mohan, L. R. Band parameters for III-V compound semiconductors and their alloys. *J. Appl. Phys.* **89**, 5815–5875 (2001).

30. Fabian, J., Matos-Abiague, A., Ertler, C., Stano, P. & Žutić, I. Semiconductor spintronics. *Acta Phys. Slov.* **57**, 565–907 (2007).

31. Seraide, R. M. & Hai, G.-Q. Low-temperature electron mobility in parabolic quantum wells. *Braz. J. Phys.* **32**, 344–346 (2002).

32. Suominen, H. J. et al. Anomalous Fraunhofer interference in epitaxial superconductor-semiconductor Josephson junctions. *Phys. Rev. B* **95**, 035307 (2017).

33. Guiducci, S. et al. Full electrostatic control of quantum interference in an extended trenched Josephson junction. *Phys. Rev. B* **99**, 235419 (2019).

34. Beenakker, C. W. J. & van Houten, H. Josephson current through a superconducting quantum point contact shorter than the coherence length. *Phys. Rev. Lett.* **66**, 3056–3059 (1991).

35. Furusaki, A. & Tsukada, M. Dc Josephson effect and Andreev reflection. *Solid State Commun.* **78**, 299–302 (1991).

36. Ideue, T. et al. Bulk rectification effect in a polar semiconductor. *Nat. Phys.* **13**, 578–583 (2017).

37. He, P. et al. Observation of out-of-plane spin texture in a SrTiO₃(111) two-dimensional electron gas. *Phys. Rev. Lett.* **120**, 266802 (2018).

Methods

Wafer growth and initial characterization. The hybrid heterostructure was epitaxially grown on an insulating InP substrate. The layer sequence featured a 100 nm $In_{0.52}Al_{0.48}As$ matched buffer, 900 nm $In_{0.52}Al_{0.48}As$ to $In_{0.84}Al_{0.16}As$ graded buffer (18×50 nm steps), a reversed 33 nm graded buffer from $In_{0.84}Al_{0.16}As$ to $In_{0.81}Al_{0.19}As$, a 25 nm $In_{0.81}Al_{0.19}As$ layer, a 4-nm-thick $In_{0.81}Ga_{0.19}As$ bottom barrier, a 7 nm InAs quantum well, a 10 nm $In_{0.8}Ga_{0.2}As$ top barrier, two monolayers of GaAs and, finally, 7 nm aluminium film as the superconductor.

The quantum well of this wafer was patterned into a top-gated Hall-bar geometry. The aluminium was selectively removed and a Ti–Au gate electrode was deposited on top of a 40 nm aluminium oxide layer. For this structure, electron mobility was measured to be 22,000 $cm^2 Vs^{-1}$ at a density $n = 0.5 \times 10^{12} cm^{-2}$ with a mean-free-path length $\ell_e \approx 270$ nm at a gate voltage $V_g = -1.8$ V. Tunnelling spectroscopy, performed on the same wafer via gate-defined quantum point contacts, revealed an induced gap $\Delta^\ast \cong 130 \mu eV$ underneath the epitaxial Al film[13].

Device fabrication. All samples were fabricated using standard electron-beam lithography techniques defining first the mesa and, in a second step, the Josephson junctions. A standard wet-etching solution (orthophosphoric acid:citric acid:hydrogen peroxide:distilled water at 1.2:22:2:88) was used to fabricate a well-defined mesa. The junctions were patterned by selective wet-etching of aluminium by using the etchant type D from the Transene Company. The remaining aluminium islands had a length of 1 μm, a width of 3.15 μm and were separated by 100 nm. A global top gate was added by covering the whole array with 40 nm aluminium oxide and 5 nm Ti/120 nm Au by atomic-layer deposition and electron-beam evaporation.

Measurements. Our measurements were performed in a dilution refrigerator. We determined the Josephson inductance by using a cold RLC resonator mounted close to the sample (for a detailed description, see ref. [13]). The device was embedded in the resonator next to a copper coil ($L_0 = 382$ nH), parallel to a capacitor ($C_0 = 4$ nF) and connected to cold ground. The whole circuit was installed on a piezo rotator with the rotation axis perpendicular to the main magnetic field. The rotation axis was such that the field of a superconducting coil always remained in the 2DEG plane. Home-made compensation coils allowed application of the desired field B_z. Alternatively, they could have been used to carefully null the magnetic-field component perpendicular to the sample plane for measurements at $B_z = 0.1$ kΩ resistors effectively decouple the resonant circuit from the external electrical environment. The centre frequency $f \equiv (2\pi\sqrt{L_T C_0})^{-1}$ of the resonance peak was used to extract the sample inductance and is given by the capacitance C_0 and the total inductance L_T, which is the sum of the external inductance L_0 and the sample inductance L. The capacitor C_0 also eliminates d.c. electric current between the cold ground and the source and voltage contacts, which allows for complementary d.c. transport measurements in the same cooldown. The resonance frequency was chosen at about 4 MHz within the range of our digital lock-in with a maximum frequency of 5 MHz. The Q factor is given by $Q = R_S^{-1}\sqrt{L_T/C_0}$ and is about 30. The damping resistance of the RLC circuit is typically of the order of 0.3 Ω. Already at sample resistances of a few ohms, the Q factor drops towards one and the resonance breaks down. Since individual junctions have a normal-state resistance of 60 Ω, a single defect within a weaker junction in our one-dimensional Josephson junction array limits the maximum bias current that we can apply before the resonance breaks down.

Band structure calculations. To deduce realistic values for the strength of the Bychkov–Rashba[38,39] and Dresselhaus[40] spin–orbit couplings arising inside the investigated InAs quantum well, and estimate their relative importance, we performed self-consistent $\mathbf{k} \cdot \mathbf{p}$ calculations. More specifically, we solved the Schrödinger–Poisson equation for conduction-band electrons within the quantum well[41–44], and accounted thereby for linear and linearized cubic spin–orbit coupling terms. Our calculations gave direct access to the spatial variations of the electrostatic potential inside the well and the related spin–orbit coupling parameters that can be used as an input for our actual transport simulation.

Transport simulations. Our transport simulations are based on the Python transport package KWANT[27]. Each InAs Josephson junction of the experimental array is described by the well-established Bogoljubov–de Gennes Hamiltonian[45], which was discretized on a generic three-dimensional tight-binding grid as inherent to KWANT's specifics. Afterwards, the system was completed by adding a fictitious vertical lead, which effectively acts as self-energy from the spectral point of view. KWANT's functionalities allowed us to invert the Bogoljubov–de Gennes matrix Hamiltonian to obtain the related Green's function and compute the Josephson current within the aforementioned self-energy lead. Following this procedure, we could derive the CPR $I(\varphi)$ of a single junction and the corresponding Josephson inductance $L(\varphi) = (\Phi_0/2\pi)[\partial I(\varphi)/\partial \varphi]^{-1}$, where $\Phi_0 = h/(2e)$ denotes the magnetic flux quantum. The inductance of the whole array is given by the single-junction inductance multiplied by the number of junctions in series. Eliminating the phase difference φ from $I(\varphi)$ and $L(\varphi)$, we can compute the

nonlinear inductance $L(I)$ and extract the supercurrent magnetochiral anisotropy parameter γ_L, as described in the main text. To obtain semiquantitative simulations we used realistic material parameters in combination with $\mathbf{k} \cdot \mathbf{p}$ calculations tailored to the experimental setup.

Data availability

The data that support the findings of this study are available at the online depository EPUB of the University of Regensburg, with the identifier doi:10.5283/epub.44877. Source data are provided with this paper.

Code availability

The computer codes that support the theoretical results, the plots within this paper and other findings of this study are available from the corresponding author upon reasonable request.

References

38. Bychkov, Y. A. & Rashba, E. I. Oscillatory effects and the magnetic susceptibility of carriers in inversion layers. *J. Phys. C.* **17**, 6039–6045 (1984).
39. Bychkov, Y. A. & Rashba, E. I. Properties of a 2D electron gas with lifted spectral degeneracy. *J. Exp. Theor. Phys. Lett.* **39**, 78–81 (1984).
40. Dresselhaus, G. Spin-orbit coupling effects in zinc blende structures. *Phys. Rev.* **100**, 580–586 (1955).
41. Calsaverini, R. S., Bernardes, E., Egues, J. C. & Loss, D. Intersubband-induced spin-orbit interaction in quantum wells. *Phys. Rev. B* **78**, 155313 (2008).
42. Fu, J. & Egues, J. C. Spin-orbit interaction in GaAs wells: from one to two subbands. *Phys. Rev. B* **91**, 075408 (2015).
43. Antipov, A. E. et al. Effects of gate-induced electric fields on semiconductor Majorana nanowires. *Phys. Rev. X* **8**, 031041 (2018).
44. Mikkelsen, A. E. G., Kotetes, P., Krogstrup, P. & Flensberg, K. Hybridization at superconductor-semiconductor interfaces. *Phys. Rev. X* **8**, 031040 (2018).
45. De Gennes, P. G. *Superconductivity of Metals and Alloys* (Addison Wesley, 1989).
46. Chen, C.-Z. et al. Asymmetric Josephson effect in inversion symmetry breaking topological materials. *Phys. Rev. B* **98**, 075430 (2018).
47. Kononov, A. et al. One-dimensional edge transport in few-layer WTe₂. *Nano Lett.* **20**, 4228–4233 (2020).
48. Wang, W. et al. Evidence for an edge supercurrent in the Weyl superconductor MoTe₂. *Science* **368**, 534–537 (2020).

Author contributions

C.B. fabricated the devices and performed the measurements. L.F. and S.R. developed and optimized the measurement method. T.L., S.G. and G.C.G. designed the heterostructure, conducted molecular-beam epitaxy growth and performed initial characterization of the hybrid superconductor/semiconductor wafer. C.B. and N.P. analysed the data. N.P. and C.S. conceived the experiment. A.C., D.K. and J.F. formulated the theoretical model. A.C. performed KWANT simulations, P.E.F.Jr. conducted the $\mathbf{k} \cdot \mathbf{p}$ calculations, C.S., J.F. and M.J.M. supervised research activities at Regensburg and Purdue, respectively. All authors contributed to discussions and to the writing of the paper.

Competing interests

The authors declare no competing interests.

Additional information

Extended data are available for this paper at https://doi.org/10.1038/s41565-021-01009-9.

Supplementary information The online version contains supplementary material available at https://doi.org/10.1038/s41565-021-01009-9.

Correspondence and requests for materials should be addressed to Nicola Paradiso.

Peer review information *Nature Nanotechnology* thanks Francesco Giazotto and the other, anonymous, reviewer(s) for their contribution to the peer review of this work.

Reprints and permissions information is available at www.nature.com/reprints.
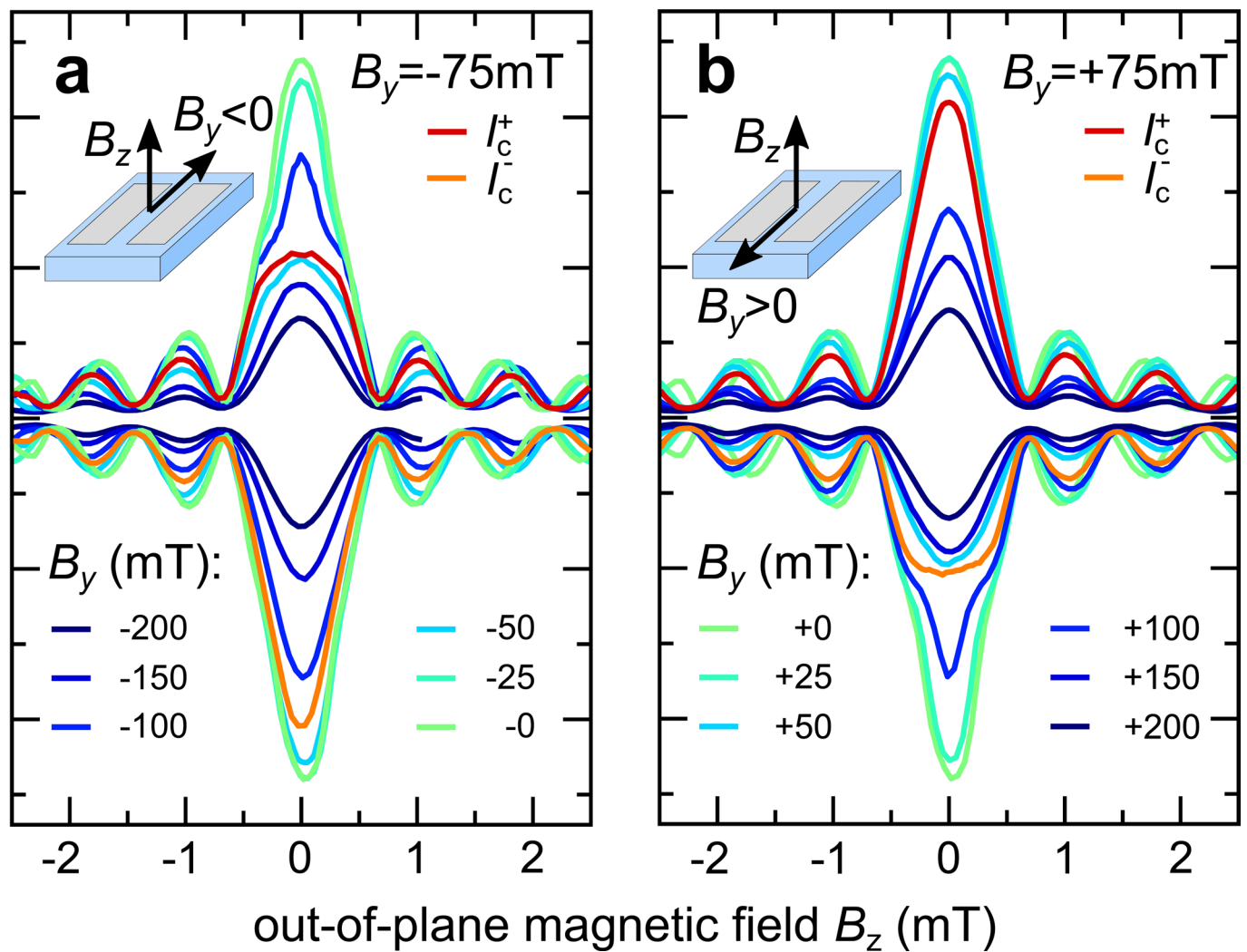
Extended Data Fig. 1 | Fraunhofer patterns with in-plane magnetic fields of opposite polarity. a, Fraunhofer patterns for the Josephson junction array, measured at $B_x = 0$ for selected values of $B_y < 0$. Compared to the patterns in Fig. 3b (here reproduced for ease of comparison in panel **b**), the B_y values are equal and opposite. Data in the two panels are not symmetric upon inversion of the current direction. Instead, each data set is mapped into the other. The system is thus symmetric upon simultaneous inversion of current and in-plane magnetic field direction. Interestingly, all the Fraunhofer patterns here reported are symmetric upon inversion of B_z. This demonstrates that the diode effect is not due to non-homogeneous supercurrent density nor to an asymmetric SQUID effect[46-48].
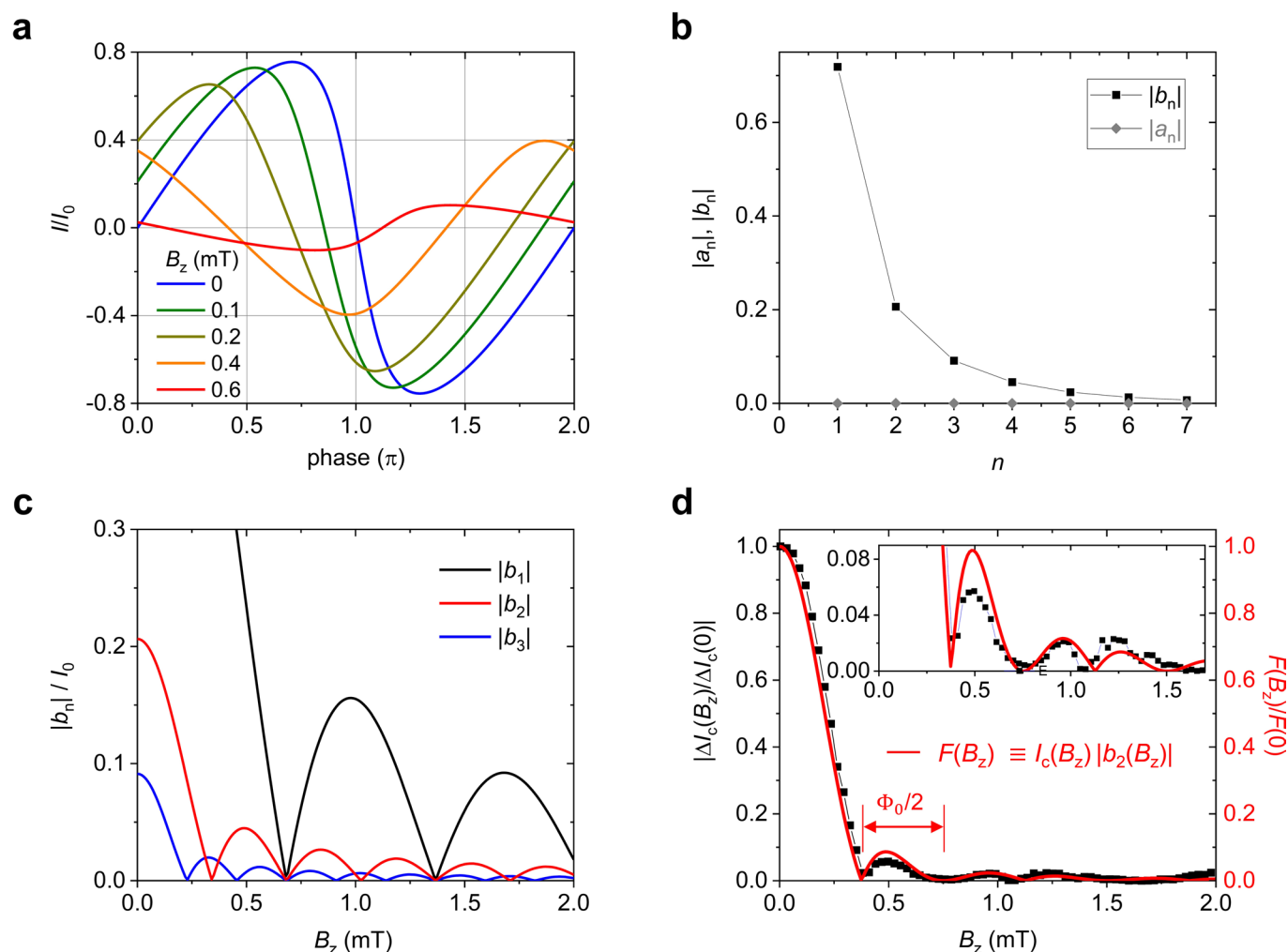
Extended Data Fig. 2 | Higher harmonics in CPR and supercurrent diode effect. a, Computed CPR for a short rectangular junction in the presence of selected value of the out-of-plane field B_z. The CPR at $B_z = 0$ is that described by the Beenakker-Furusaki equation with the parameters characterized in Ref. [13]. **b,** Modulus of the first seven Fourier sine (b_n) and cosine (a_n) coefficients for the $B_z = 0$ CPR. **c,** Out-of-plane magnetic field dependence of the modulus of the first three sine coefficients. **d,** Absolute value of the difference between the measured critical currents in the two direction for $B_y = 75$ mT (black symbols). Data are normalized to the value at $B_z = 0$. The graph refers to the same data as in Fig. 3d. The experimental values are in good approximation described by the product of the critical current I_c and the modulus of the second Fourier coefficient $|b_2|$ (red line), both computed as a function of B_z. The former factor describes the magnitude of the critical current as a whole, while the latter quantifies how skewed the CPR is, and therefore the strength of the diode effect. Notice that the product $I_c|b_2|$ makes clear why the measured critical current difference goes to zero (i) for multiples of half flux quanta $\Phi_0/2$ and (ii) with (alternately) cusp-like and parabolic-like minima.